A Study of Tau Identification with the CMS Detector at the LHC

by

Philip James Ilten

Submitted to the Department of Physics
in partial fulfillment of the requirements for the degree of

Bachelor of Science

at the

MASSACHUSETTS INSTITUTE OF TECHNOLOGY

June 2008

© Philip James Ilten, MMVIII. All rights reserved.

Author . . . .
Department of Physics
May 10, 2008

Certified by . . . .
Christoph M. E. Paus
Associate Professor
Thesis Supervisor

Accepted by . . . .
David E. Pritchard
Senior Thesis Coordinator, Department of Physics
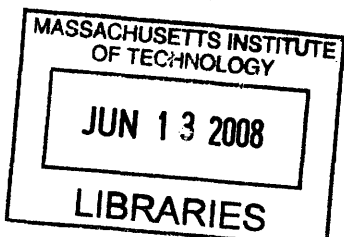
A Study of Tau Identification with the CMS Detector at the LHC

by

Philip James Ilten

Submitted to the Department of Physics
on May 13, 2008, in partial fulfillment of the
requirements for the degree of
Bachelor of Science

Abstract

In this thesis I explore the identification of τ leptons from simulated reconstructed data that will be collected by the Compact Muon Solenoid (CMS) detector on the Large Hadron Collider (LHC) at CERN. The two components of particle identification, efficiencies of τ identification from generator level information, along with fake rates of the current default algorithm have been determined and analyzed for a photon plus jets background sample and QCD background sample. I propose a new τ lepton identification algorithm that employs a signal cone parametrized with respect to the τ transverse energy, and an isolation cone parametrized with respect to charged particle density surrounding the τ jet. Using the default algorithm an efficiency of 27.7% is achieved along with a photon plus jets fake rate of 1.96%. Using the proposed algorithm and matching the efficiency of the default algorithm, an efficiency of 26.9% and a fake rate of 0.44% is achieved. Approximately matching fake rates, an efficiency of 37.4% is achieved with a fake rate of 2.36%.

Thesis Supervisor: Christoph M. E. Paus
Title: Associate Professor

Acknowledgments

This thesis is dedicated to my father, Mark Ilten.

I would like to express my deepest thanks to Professor Christoph Paus who has taught me more in two summers then my entire career at MIT. The opportunities and experiences that Christoph has given me are the chances of a lifetime.

I would also like to give a special thanks to Professor Markus Klute who has always had the time to answer the questions of an undergraduate, despite his busy schedule. Markus has always encouraged me to think on my own and question the status quo. Without him, this thesis would not have been possible.

I owe a debt of gratitude to my academic adviser at MIT, Professor Bolek Wyslouch and would like to thank the entire MIT physics group at CERN, specifically Professor Steve Nahn, Guillelmo Gomez-Ceballos, Mike Miller, Jonaton Piedra and my fellow undergraduates Michael Mooney and Costantinos Melachrinos. Throughout my career at MIT my family has given me loving support; Jennifer, Adam, Nathan, Carla, and Karen. I would like to thank my roommate Akil Middleton along with Éadaoin McClean for keeping me sane throughout my senior year. Finally I would like to thank the brothers of Zeta Psi.

Contents

5 Conclusion

Chapter 1

Introduction

Beginning with the discovery of the electron, physicists have been developing a theory to describe the interactions between particles, which in its most up-to-date form is called the Standard Model of particle physics. Within the Standard Model there are two types of particles, fermions and bosons. Fermions are the constituents of all matter, while bosons are the sources of the fields through which fermions interact. Despite being one of the most complete scientific theories in existence, the Standard Model remains incomplete with many open questions, including how to incorporate gravity, the mass of neutrinos, the Higgs boson, and the origin of arbitrary constants. Many of these questions cannot be explained through the Standard Model, and require extensions such as super symmetry, or even entirely new theories such as string theory [1].

The Large Hadron Collider (LHC) at CERN with its unprecedented 14 TeV energy is expected to produce new physics that will either challenge or validate the Standard Model. One of these physics searches is for the theoretical Higgs boson, a particle needed by the Standard Model for the masses of particles. While the LHC is not scheduled to begin data taking operations until Summer of 2008, detailed simulations are being run to prepare for actual detector data. To facilitate preparation for the Higgs search, this paper analyzes the underlying properties of τ jets within the Compact Muon Solenoid (CMS) detector, on both generator and reconstructed levels, using Monte Carlo simulation techniques.

An important final state in searches for the Higgs boson in the Standard Model and super symmetric extensions is its decay into τ pairs. However, unlike other charged leptons, τ particles decay into lighter hadrons and leptons making identification of τ's within particle detectors more challenging. The τ particle primarily decays into highly collimated jets of one or three charged particles consisting of lighter leptons or hadrons along with their corresponding neutrinos. In both one and three prong hadronic decays the underlying kinematics of the physics event allows for unique identification of τ jets.

In this paper the Z boson decay $Z \rightarrow \tau^+\tau^-$ is studied because it provides one of the cleanest known decays into a τ lepton pair. The underlying event topology is examined and compared to primary background topologies in an effort to allow for differentiation between signal and background. Specifically, the shape of the hadronic τ jet is investigated, including possible parametrization. Observables such as transverse momentum, impact parameter, etc. along with new jet finding methods are examined to provide a framework for high level trigger and cut-based analysis on reconstructed level data.

This paper is written to be self-contained yet to give the reader a full appreciation of the original analysis performed. Section 2 gives a brief framework for the theory behind this paper followed by an overview of the experimental setup in Section 3. This section is broken into two parts, Section 3.1 describing the LHC and Section 3.2 describing the CMS detector. Next, the method for identifying τ leptons within the CMS detector is given in Section 3.3. Sections 4 and 5 conclude the paper by comparing the performance of current default algorithms and the new algorithm proposed within this paper. All units are "God-given", where $q = \hbar = c = 1$.

Chapter 2

Theory

The Standard Model, developed during the late 1960's and early 1970's has played a critical role in shaping the face of particle physics for the past 40 years. Considered to be one of the most complete scientific theories, the Standard Model has the ability to predict the interactions of fundamental particles through three of the four fundamental forces: electromagnetic, weak, and strong. Nearly every discovery in particle physics since the development of the Standard Model has been predicted by it, including the discovery of the W and Z bosons in 1983 at the Super Proton Synchrotron (SPS), the discovery of the gluon in 1979 at DESY, the discovery of the charm quark in 1974 at Brookhaven National Laboratories (BNL) and the Stanford Linear Collider (SLAC), and the more recent discovery of the top quark in 1995 by the Collider Detector at Fermilab (CDF) and DØ.

2.1 The Standard Model

Standard Model particles consist of spin 1/2 particles called fermions and force carrying particles called bosons. On the left of Figure 2-1 all fermions are shown in green and blue. Fermions can further be split into leptons, shown in blue, and quarks, shown in green. On the right in orange are the three fundamental forces of the Standard Model along with their force carrying bosons. The electromagnetic force is carried by the photon, the weak force by the W and Z bosons, and the strong force by the

gluon. At high energies the electromagnetic force and weak force combine to create the electroweak force which is described through Quantum Electrodynamics (QED).

Leptons are further subdivided into chargeless leptons and charged leptons. Oftentimes the leptons are split into three levels arranged from lowest mass and earliest discovery (the electron) to heaviest mass and latest discovery (the τ lepton). To illustrate these levels, the leptons are arranged accordingly in Figure 2-1. The charged leptons consist of the electron, muon, and τ lepton all of which have charge negative one. Corresponding to each charged lepton is a chargeless lepton, or neutrino. They are the electron neutrino, muon neutrino, and τ neutrino. Unlike the charged leptons, neutrinos have very small masses, which have yet to be measured experimentally, although the mass differences between neutrinos are known [2]. Both charged and chargeless leptons interact through the weak force, but do not interact through the strong force. The charged leptons, like all charged particles, also interact through the electromagnetic force.

Quarks are non-integer charged particles that interact with all three forces. Just as there are three levels of leptons corresponding to both mass and discovery, there are analogous levels for the quarks. Quarks, unlike leptons, interact with the strong force. Subsequently, quarks without partners, or unconfined quarks, are not found in nature. The confinement of quarks to groups makes experimental mass measurements difficult, so mass ranges rather then specific masses are assigned to each quark. The quarks are split into two groups of charge, charge plus two thirds and charge minus one third. The charge plus two thirds quarks are up type quarks and are called up, charm, and top quarks. Quarks with charge minus one third are down type quarks and are called down, strange, and bottom quarks. Quarks interact through Quantum Chromodynamics (QCD), where each quark has a color of green, blue, or red, similar to electric charge in electrodynamics.

All fermions, both quarks and leptons, have anti-particles with a corresponding anti-charge and anti-color. A red up quark with charge plus two thirds, for example, has a corresponding anti-particle of color anti-red and charge negative two thirds. Combinations of quarks and anti-quarks combine to create hadrons. All experimen-

Fermions				Bosons	Forces
Leptons		**Quarks**			
Charge -1	Charge 0	Charge $+\frac{2}{3}$	Charge $-\frac{1}{3}$	Photon γ 0 GeV	Electro—magnetic
Electron e 0.51 MeV	Electron Neutrino ν_e	Up u 1.5–3 MeV	Down d 3–7 MeV	W Boson W^+, W^- 80.4 GeV	Weak
Muon μ 105.7 MeV	Muon Neutrino ν_μ	Charm c 1.2 GeV	Strange s 95 MeV	Z Boson Z^0 91.2 GeV	
Tau τ 1.8 GeV	Tau Neutrino ν_τ	Top t 172 GeV	Bottom b 4.2 GeV	Gluon g 0 GeV	Strong

Figure 2-1: Diagram of the fundamental constituents of the Standard Model. Each box representing a particle gives the name, symbol, and mass (excluding neutrinos). All mass data is taken from Reference [3]. On the left are the fermions, leptons in blue and quarks in green. On the right are the forces, coupled with their boson carriers.

tally observed hadrons are either quark anti-quark combinations, mesons, or three quark combinations, baryons. The proton is a baryon which consists of two up quarks and one down quark, *uud*. Similarly the neutron is also a baryon and consists of two down quarks and one up quark, *ddu*.

The mathematical framework for the Standard Model consists of Quantum Field Theory (QFT) which describes each particle and force as a field. While complex systems cannot be solved directly using QFT, many simple systems of particles and their interactions can.

2.2   The Higgs Boson

Despite its predictive power, the Standard Model is not experimentally complete and requires further experimental confirmation. The Standard Model, through $SU(2) \times$

$U(1)$ gauge theory predicts the existence of the W and Z bosons. Gauge theories, however require that bosons described by them, such as the photon, are massless. In the case of the W and Z bosons, both are experimentally verified to have masses, which are theoretically predicted through the "Higgs Mechanism".

The "Higgs Mechanism", spontaneously breaks the $SU(2) \times U(1)$ symmetry through a non-zero vacuum expectation value and gives the W and Z bosons mass. The theory introduces a Higgs field with four degrees of freedom, where three degrees are absorbed by the masses of the W and Z bosons. The remaining degree of freedom should result in an experimentally observable Higgs boson [4]. Accordingly, experimental searches have been made but with no observed result.

The mass of the SM Higgs boson is given by Equation 2.1, where v is the vacuum expectation value of the Higgs field, and λ the quartic Higgs self-coupling [3].

$$M_H = v\sqrt{2\lambda} \tag{2.1}$$

The value for v is given by Equation 2.2 where G_F is the measured Fermi coupling constant. The constant gives the strength of the weak force between fermions and is experimentally determined from the lifetime of a muon [5].

$$v = \left(\sqrt{2}G_F\right)^{-1/2} \approx 247\,\text{GeV} \tag{2.2}$$

The value for λ, however, is free, and subsequently the mass for the SM Higgs boson is not predicted. If the SM is to be maintained as a perturbation theory, the value of λ is limited, which implies an upper bound on the mass of the SM Higgs boson. Higgs boson searches at the Tevatron and the Large Electron Positron collider place a lower limit on the SM Higgs boson at $M_H > 114.4$ GeV within a 95% confidence level [6]. In higher order calculations the Higgs boson couples with various particles and so an upper limit can be placed through measurements of these observables. Precision measurements on electroweak observables and the top quark mass place an upper limit of $M_H < 160$ GeV, also within a confidence level of 95% [6].
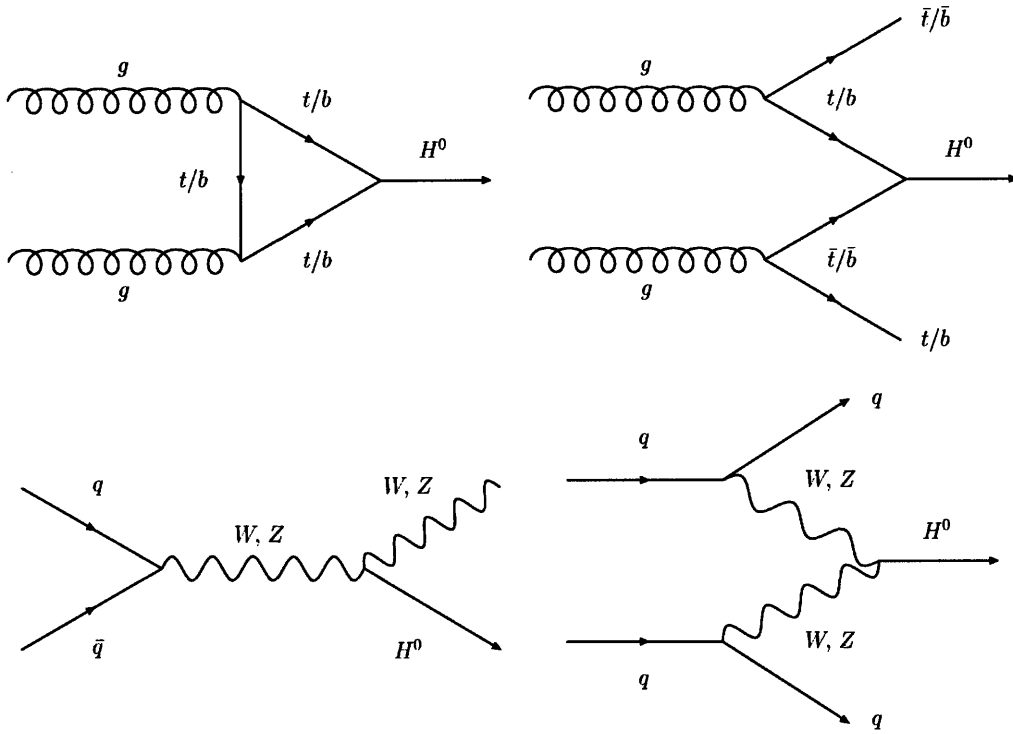
Figure 2-2: The four primary production mechanisms of the Standard Model Higgs boson at the Large Hadron Collider.

Production of the Higgs boson is possible through a variety of mechanisms, but the four most important candidates for a pp collider such as the LHC are shown in Figure 2-2. The upper left diagram depicts gluon-gluon fusion, the upper right demonstrates associated top-quark production, the lower left shows associated W production, and the lower right gives weak-boson fusion. The cross sections of the different diagrams are shown on the bottom of Figure 2-3. Notice that the two largest production mechanisms, by significance of cross section, are gluon-gluon fusion and weak-boson fusion.

The Higgs boson, like all other bosons, has a very short life, so direct detection of the particle is impossible. The decay products of the Higgs boson must be reconstructed to observe the presence of a Higgs boson. Because this type of analysis depends entirely upon the decay products of the Higgs boson, it is important to know

the subsequent branching ratios. The top plot of Figure 2-3 shows the most common branching ratios for a SM Higgs boson versus the theoretical mass of the Higgs boson [7].

In the lower mass range of the Higgs boson ($M_H \lesssim 135$ GeV) the two largest branching ratios are $H \rightarrow b\bar{b}$ and $H \rightarrow \tau^+\tau^-$. However, the $b\bar{b}$ channel, indicated in red in the top plot of Figure 2-3, is difficult to analyze within a hadron collider environment due to large backgrounds. The $H \rightarrow \tau^+\tau^-$ channel, indicated in green, on the other hand, is a cleaner signal then the $H \rightarrow b\bar{b}$ channel, with a manageable background. Combining this cleaner signal with the signature of weak-boson fusion Higgs production makes this an important discovery channel. Therefore, proper τ identification in the CMS detector is of paramount importance to the discovery or exclusion of the SM Higgs boson.

2.3   The τ Lepton

The τ lepton is the heaviest of the three charged leptons: e, μ, and τ. The electron is stable as there are no lighter particles to which it can decay. The muon which decays into an electron, $\bar{\nu}_e$, and ν_μ has a lifetime of 2.2×10^{-6} seconds. The τ also decays, but does so more quickly, with a lifetime of 3.0×10^{-13} seconds. Since the τ is more massive then e, μ, and various lighter hadrons such as π's and K's, it has a variety of decay channels available. Table 2.1 gives a brief outline of the primary decay channels for the τ. In this table, h stands for hadron and ℓ for lepton.

It is convenient to divide the primary decay channels into decays with one charged particle, or a one prong decay, and three charged particles, or a three prong decay. A channel with five charged particles also exists, but contributes less then 1% of all channels. In all of the decay channels however, the number of daughter particles is always greater then one. Subsequently all τ decays are called τ jets and it is the characteristic properties of τ jets that make identification of τ leptons in particle detectors possible.

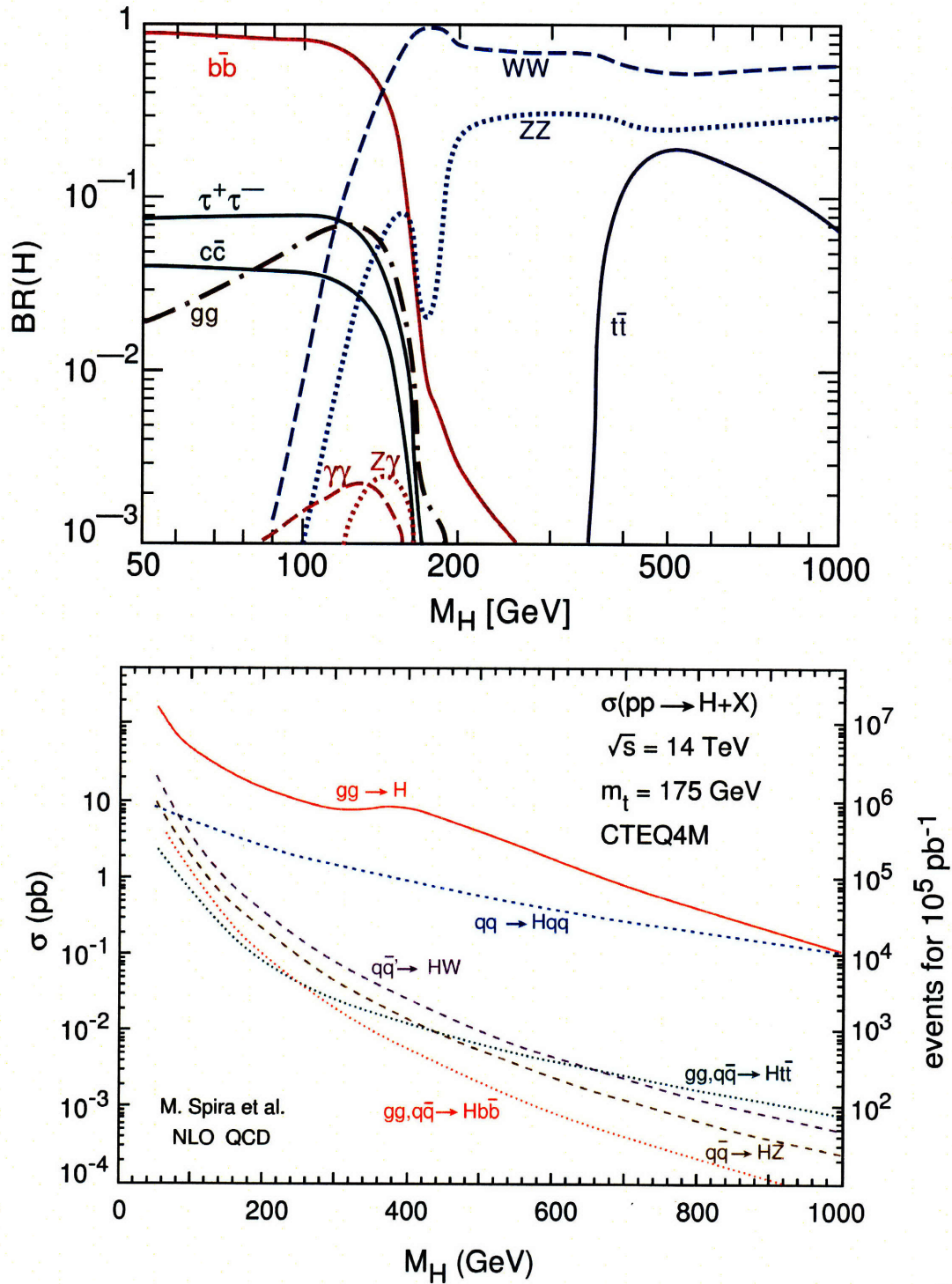The most probable decay of a τ lepton, occurring in 37% of all decays, is a charged

16

Figure 2-3: The theoretical branching ratios for the SM Higgs boson from Reference [7] are shown in the top plot. The theoretical cross sections for Higgs boson production at the LHC from Reference [8] are shown in the bottom plot.

Channel	Percent	
one charged particle		
$\Rightarrow h^- h^0 \geq 1\, \nu_\tau$	37%	
$\Rightarrow \ell^- \bar{\nu}_\ell \nu_\tau$	35%	85%
$\Rightarrow h^- \nu_\tau$	12%	
three charged particles		
$\Rightarrow h^- h^- h^+ \nu_\tau$	10%	
$\Rightarrow h^- h^- h^+ h^0 \geq 1\, \nu_\tau$	5%	15%
five charged particles	< 1%	

Table 2.1: Primary decay channels of the τ lepton. Data is taken from Reference [3].
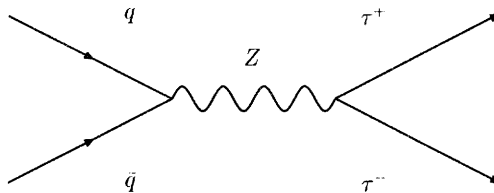

Figure 2-4: Diagram of the Drell-Yan production of τ leptons.

hadron, a τ neutrino, and one or more neutral hadrons. Occurring in 35% of all decays is the second most probable channel, consisting of a τ neutrino, a lepton, and its corresponding anti-neutrino. Next, 12% of all τ leptons decay into a a τ neutrino and a charged hadron. Combined, these three channels account for 85% of all τ lepton decays, and are all one prong decays.

For 10% of all decays, the τ lepton decays into one τ neutrino and three charged hadrons, and another 5% with additional neutral hadrons. These two channels combined account for 15% of all τ lepton decays, and are both three prong decays.

Notice that for further discussion three primary types of τ jets are considered, a one prong lepton jet, a one prong hadron jet, and a three prong hadron jet. The one prong lepton jet is not explored in this paper because such a jet is identified as an electron or muon by the CMS algorithms. This leaves the one prong and three prong hadronic channels.

All these channels produce highly collimated jets with unique topologies that are analyzed in Section 4 of this paper. However, to study τ jet behavior and topology

in data, a clean, easily available signal, similar to a potential Higgs boson signal, must be used. The Drell-Yan production and subsequent decay of a Z boson is such a calibration signal. The τ leptons from this process, shown in Figure 2-4, are the subject of this analysis.

Chapter 3

Experiment

The Large Hadron Collider (LHC) is a proton-proton collider located at the European Organization for Nuclear Research (CERN) in Geneva, Switzerland. Construction of the LHC began in 1994 with approval from the CERN Council for a two stage development plan. The first stage consisted of a 10 TeV center-of-mass collider set to be operational in 2004 followed by a subsequent upgrade of the collider to a 14 TeV center-of-mass in 2008. However, additional funding from non-member states of CERN, primarily the United States, Canada, India, Russia and Japan, allowed for the elimination of the 10 TeV development stage and direct construction of the final 14 TeV stage. Construction delays however have pushed the initial 2004 completion date to 2008 or later. Full details on the LHC and its detectors are given in the *LHC Design Report* [9].

3.1   Large Hadron Collider

The LHC is designed specifically to search for Standard Model and rare physics events at energies of up to 14 TeV and does so through two large multi-purpose detectors, the Compact Muon Solenoid (CMS) and A Toroidal LHC Apparatus (ATLAS). To observe rare physics events through these detectors a significant number of events must be recorded. Here the number of events for a given physics process, N_{event}, is given by the luminosity of the collider beam, $\mathcal{L}$, multiplied by the cross section of the

process, σ_{event} [10].

$$N_{\text{event}} = \mathcal{L} \, \sigma_{\text{event}} \tag{3.1}$$

From Equation 3.1 it is apparent that rare physics processes with small cross-sections will not be observed in either of the two detectors unless a high beam luminosity can be provided by the accelerator. Beam luminosity is proportional to the number of bunches in the beam n_{b}, number of particles per bunch N_{b}, the relativistic factor γ, and the frequency of the beam f. In Equation 3.3 the relation for luminosity is shown, where β^* is the beta function at the collision point,

$$\beta^*(x,y) = \frac{1}{y} \sum_{n=0}^{\infty} (-1)^n \frac{y^{n+1}}{n!(x+n)} \tag{3.2}$$

and ϵ_{n} is a normalization factor. The second product of Equation 3.3 corrects for the crossing of the two beams at the interaction point with angle θ_{c}, RMS bunch length σ_z, and transverse RMS beam size σ^* [10].

$$\mathcal{L} = \frac{n_{\text{b}} N_{\text{b}} \gamma f}{4\pi \epsilon_{\text{n}} \beta^*} \left[1 + \left(\frac{\theta_{\text{c}} \sigma_z}{2\sigma^*} \right) \right]^{-1/2} \tag{3.3}$$

Beam frequency and interaction point crossing angles are limited by current technology so a large number of particles must be used to maintain a high luminosity. Creation of anti-protons in large quantities is difficult, and at large energies, qq and $q\bar{q}$ cross sections are similar. Consequently, proton-proton collisions are used to maintain a high luminosity. The LHC creates two proton beams by using a dual magnet system that circulates the beams in opposite directions. The LHC is housed in the old tunnels for the Large Electron Positron Collider (LEP). Because the LEP needed only one vacuum and magnet system for both beams, the beam channels of the LHC, which require independent magnet systems, have been designed to fit within a single cryostat structure that fits within the space constraints of the old LEP tunnel system.

The proton beams are prepared to enter the main ring as shown in Figure 3-1 by first passing through the linear accelerator Linac2, the Proton Synchrotron Booster,
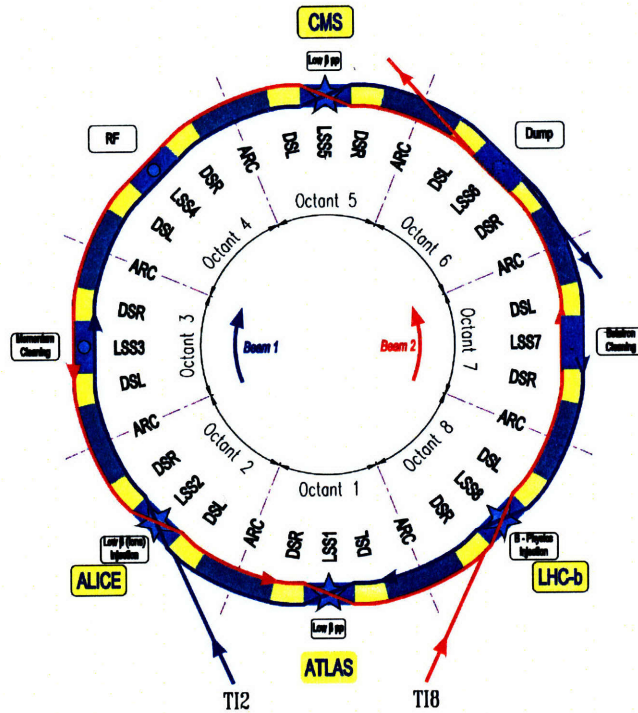
Figure 3-1: Schematic of the LHC, modified from Reference [9].

the Proton Synchrotron, and finally the Super Proton Synchrotron. The main LHC ring consists of eight curved sections labeled octants 1 through 8 in Figure 3-1. Between each arc is a straight length of tunnel or point, each utilized for experimental or utility installations. At four of these points, marked with stars, beam crossings occur and are the locations of ATLAS (point 1), ALICE (point 2), CMS (point 5), and LHC-b (point 8). Beam insertions occur at points 2 and 8, while points 3 and 7 contain beam collimators, point 4 contains the RF system, and point 6 houses two independent beam dumps.

Upon initial start-up the LHC will not operate at its peak luminosity, but after subsequent testing will be ramped to peak. A full set of relevant beam parameters are found in Reference [11]. The expected peak operational luminosity for the CMS detector is 10^{34} cm^{-2}s^{-1}.

23

3.2 CMS Detector

The CMS detector, shown in Figure 3-2 is a compact detector consisting of a 4 Tesla superconducting solenoid surrounded by 4 sub-detectors: a silicon tracker, an electromagnetic calorimeter (ECAL), a hadronic calorimeter (HCAL), and muon chambers. The layout of the CMS detector is designed specifically to perform well in the areas of muon detection, di-muon mass reconstruction, momentum resolution, electromagnetic energy resolution, missing energy resolution, and reconstruction efficiency of particles passing through the detector [12].

The origin of the CMS coordinate system is given by the nominal interaction point. The longitudinal or beam axis of the detector as shown at the bottom of Figure 3-2 is identified as the z-axis, which passes through the origin. The y-axis points upwards towards the surface and the x-axis points inwards to the center of the LHC. Using a Cartesian coordinate system complicates particle representation, so a combination of cylindrical and spherical coordinates are used instead. The traditional cylindrical coordinate definition of r defines the radial distance from the z-axis. The spherical coordinate parameter ϕ defines the angle between a radius from the origin and the y-axis. Similarly the spherical coordinate θ defines the angle between a radius from the origin in the xz-plane and the x-axis. The range of ϕ and θ is $-\pi/2$ to $\pi/2$. However, θ is rarely used and pseudo-rapidity, η, which is Lorentz invariant for massless particles, is used instead. Pseudo-rapidity is defined in terms of θ in Equation 3.4.

$$\eta \equiv -\ln\left[\tan\left(\frac{\theta}{2}\right)\right] \tag{3.4}$$

The inner most layer of the detector is the silicon tracker represented by concentric red circles of the top view of Figure 3-2. A longitudinal view of an upper quarter of the tracker is given by the dark and light red rectangles located in the lower right portion of the bottom view of Figure 3-2. Because the τ has a very short lifetime of $(290.6 \pm 1.0) \times 10^{-15}$ seconds it subsequently has a very small impact parameter, the distance from the origin at which the τ lepton decays, of 87.11 μm [3]. This means that τ's created at the interaction point will have decayed to daughter particles, as
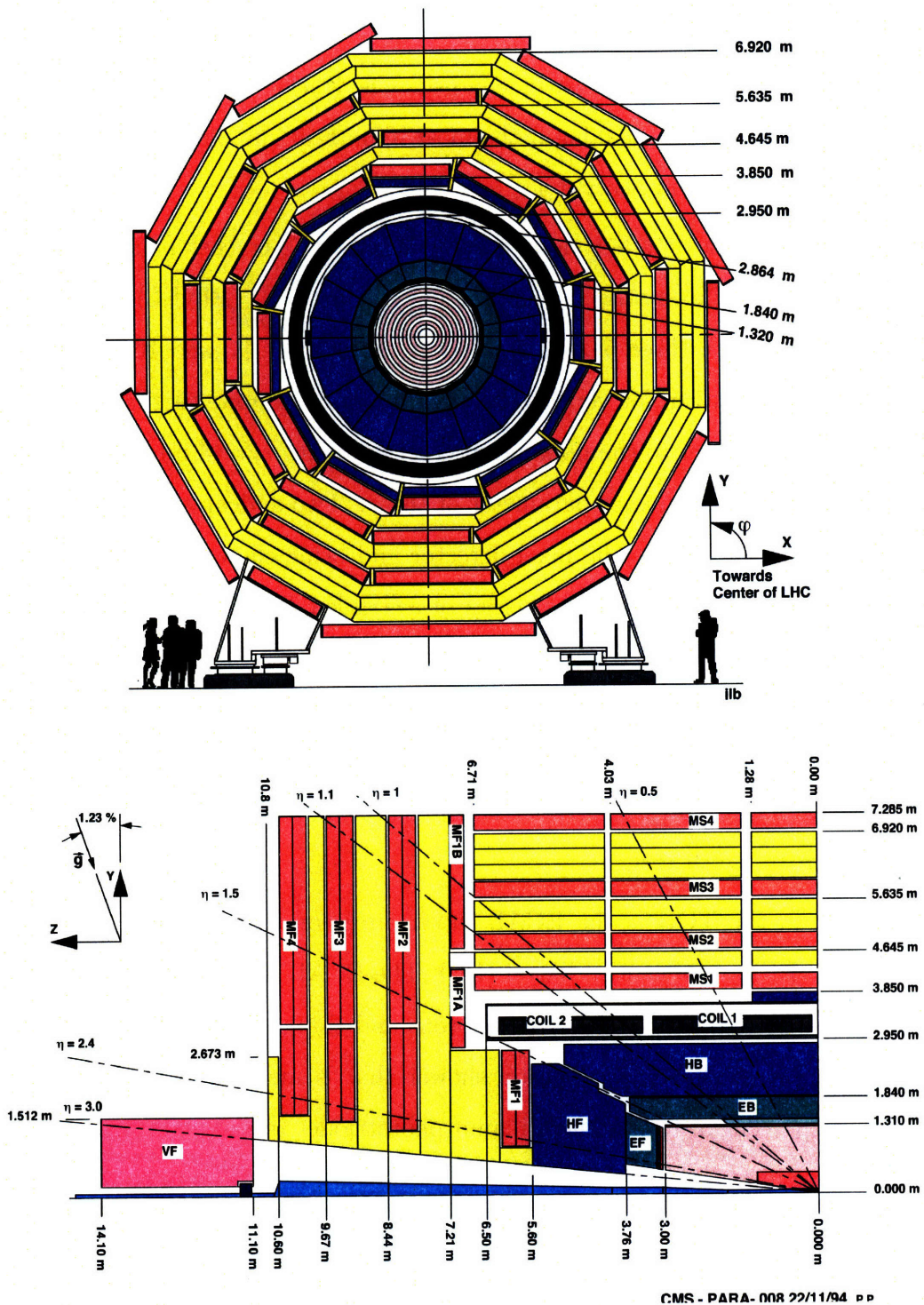
Figure 3-2: From top to bottom, transverse and one quarter longitudinal view of the CMS detector from Reference [13].

discussed in Section 2, before reaching the innermost layer of the pixel detector or the beamline. However, by charge conservation, and as show in Table 2.1, at least one of the daughters of the τ must be charged. The tracker is able to reconstruct the paths of charged particles, making it the most important sub-detector for identifying τ leptons as will be see in Section 4.

Figure 3-3 gives a detailed view of the tracker. The tracker itself consists of a pixel detector and silicon strip tracker. The pixel detector (PIXEL) surrounds the interaction point with three barrels located at radii of 44, 73, and 102 mm, making the pixel detector critical for vertex extrapolation. Notice however that the distance of the closest pixel layer to the nominal interaction point, $r = 44$ mm, is significantly larger then that of the impact parameter of the τ. Two endcap disks on either side of the pixel barrel complete the pixel detector and bring the total pixel count to 66 million pixels. The strip tracker consists of a Tracker Inner Barrel (TIB), Tracker Outer Barrel (TOB), Tracker Inner Disks (TID), and Tracker EndCaps (TEC) shown in Figure 3-3. The TIB has a single point resolution of 230 μm while the TOB has a single point resolution of 530 μm [12]. The geometry of the tracker is designed specifically so that for any charged particle nine hits are attained in the fiducial region of the tracker, $|\eta| \leq 2.4$ [12].

Adjacent to the TOB is the ECAL shown in green in Figure 3-2 consisting of two endcaps (EF) and a central barrel (EB). The ECAL is composed of $61,200$ lead tungstate (PbWO$_4$) crystals. Incident photons and charged particles cause the crystals to scintillate and create a photon shower that is measured by avalanche photodiodes in the central barrel and vacuum phototriodes in the endcaps. The use of lead tungstate helps achieve a high crystal density which results in an accurate and radiation resistant calorimeter. The central barrel covers a fiducial region of $|\eta| < 1.5$ and the endcaps a region of $1.5 < |\eta| < 3.0$ [14].

Complementing the ECAL is the HCAL represented in blue in Figure 3-2. The HCAL's primary purpose is to measure energy deposited from hadronic jets and record missing transverse energy from neutrinos. The HCAL's ability to measure jet energies plays an important role in τ identification as discussed in Section 3.3. The HCAL
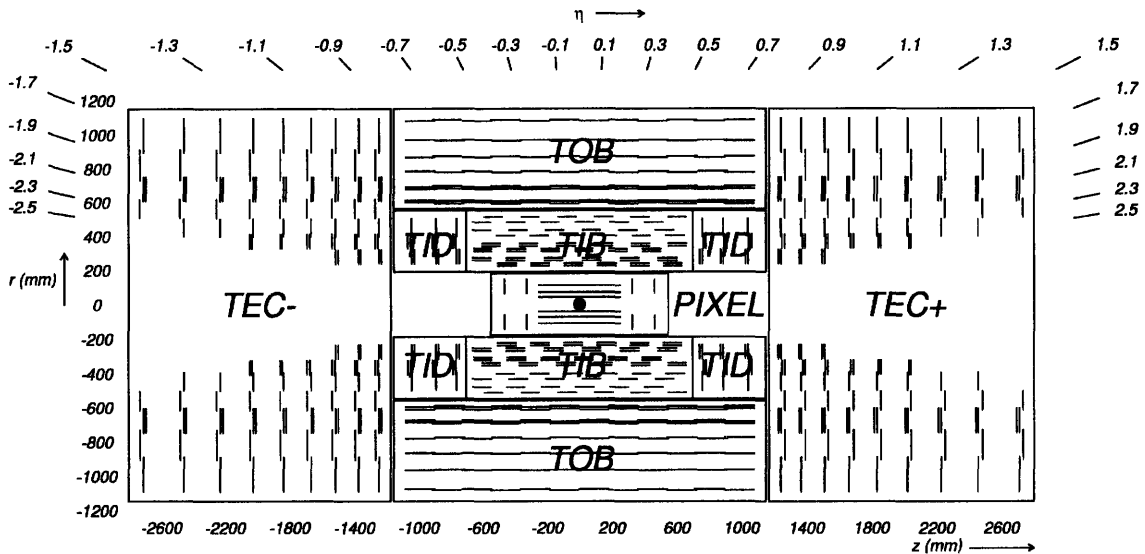
Figure 3-3: Detailed longitudinal schematic of the silicon tracker, located at the center of the CMS detector [12].

consists of a central barrel (HB) and an endcap (HF) along with an outer hadron calorimeter or tail catcher. The tail catcher is shown in blue just above COIL1 of the superconducting solenoid at $r = 3.9$ m and $y = 3.85$ m at the bottom of Figure 3-2. Each layer is composed of plastic scintillation tiles covered with a brass or steel casing which feed though optic channels into hybrid photodiodes. With these three layers of approximately $70,000$ tiles, the HCAL covers a large fiducial region of $|\eta| < 5.2$ [12].

The final three sections of the CMS detector are the trigger system, the superconducting solenoid, and the muon chambers. Due to the importance of the trigger system to τ lepton identification, it is fully described in Section 3.3. The superconducting solenoid is shown in gray in Figure 3-2 while the muon chambers surround the detector and are colored yellow and red. The solenoid is composed of four windings of a NbTi conductor and must be maintained at a temperature of 4.6 K while in operation. At full power the solenoid reaches a field of 4 T and a total stored energy of 2.6 GJ [15]. This provides a sufficiently large magnetic field to visibly deflect the paths of charged particles with high transverse momenta. The final section of the detector, the muon chambers, give a clean method for identifying muons. Muon detection however is not critical in the following and will not be further discussed. A
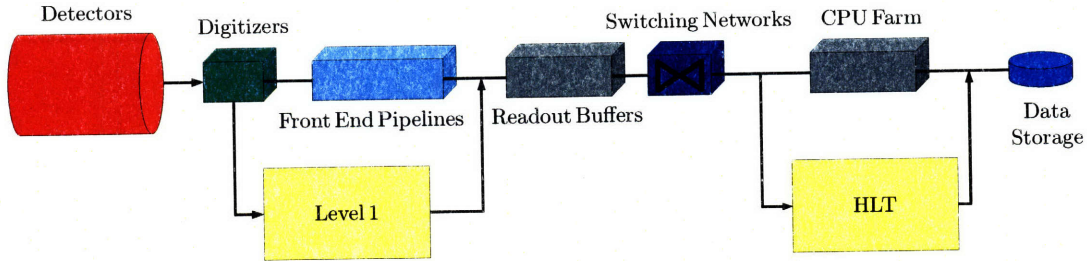
27

Figure 3-4: Architecture of the trigger system adapted from Reference [16].

reference and full description of muon identification is given in Reference [15].

3.3 CMS Trigger

Only a small fraction of the events observed within the CMS detector are of interest for current studies. Accordingly the CMS detector has a very high input data rate of 40 MHz and must filter this to a more manageable level of about 100 Hz to make data storage and analysis feasible [16]. For CMS, the trigger selection process must choose on the order of 1 event for every 10^5 events received by the triggers [17].

A diagram of the full trigger architecture, adapted from Reference [16], is shown in Figure 3-4. Events are output from the detector at a rate of 40 MHz which is reduced to a rate of 100 kHz by the Level 1 trigger consisting of custom made processors. The Level 1 trigger has a 3 μs latency, during which the the data is retained in the front-end pipelines. Events are then built by a switching network and passed to the High Level Trigger (HLT). The HLT is built entirely of commercial processors allowing the system to be adapted as both technology and software improve over time [16].

3.3.1 Level 1 τ Trigger

The Level 1 trigger is split into the calorimeter trigger and the muon trigger. The calorimeter trigger is then split into a general trigger, and a jet trigger. The jet trigger identifies three types of jets: center, forward, and τ jets and is critical to

the identification of $H \to \gamma\gamma$ and $H \to \tau^-\tau^+$ events. Because 65% of τ decays are hadronic jets with at least one charged particle, both the ECAL and HCAL readouts are well suited for not only the Level 1 trigger, but the seeding of the HLT.

The Level 1 calorimeter trigger begins by creating trigger towers which correspond to a 5×5 crystal cluster in the ECAL and a single readout from the HCAL. The energy of each trigger tower is summed and digitized by trigger primitive generator circuits from each calorimeter cell. The digitized trigger tower energies are passed to custom processors built of application-specific integrated circuits, which for the τ jet trigger group the trigger towers into 4×4 clusters as shown in Figure 3-5.

The processor algorithm then groups 4×4 clusters of trigger towers into a 12×12 array. The center of the array, or active cluster, is a 4×4 cluster where the summed energy of the 16 trigger towers within it is greater then the energies of all the surrounding 4×4 clusters. In Figure 3-5 the active cluster is located within the ECAL and is shown in blue.

Next, each inactive 4×4 cluster is examined for "τ-veto bits", where a veto bit is a specific pattern of "active" trigger towers. Trigger towers are labeled "active" if their transverse energy is greater then 2 GeV and are shown in red. The τ-veto bits are specific active trigger tower patterns which are determined by simulation from the topology of τ jets within the calorimeters. The current τ-veto bits are shown on the right of Figure 3-5.

If a τ-veto bit is found within a 4×4 cluster, then the entire 12×12 array is rejected as a possible τ jet candidate and the data from the detector is not passed on to the HLT. If all 9 of the 4×4 clusters within the 12×12 array are free of τ-veto bits, then the event is passed to the HLT [18]. In the example of Figure 3-5 a τ-veto bit is located in the upper right 4×4 cluster, so this event would not be passed on.

3.3.2 High Level τ Trigger

After passing through the Level 1 trigger the data rate is reduced to 100 kHz, input to the switching network, and passed to the HLT. The HLT is a CPU farm made from commercially available machines, so it is easily replaced and updated. Virtual trigger
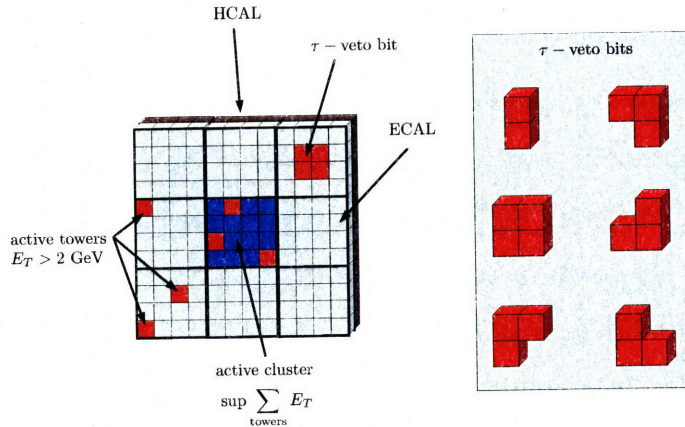
Figure 3-5: Level 1 τ jet trigger algorithm. Gray designates the ECAL, brown the HCAL, blue the active cluster, and red active bits.

names are assigned to various steps of the HLT algorithm. Level 2 utilizes Level 1 calorimeter and muon chamber information. Level 2.5 includes pixel detector data, and Level 3 utilizes all available data including full tracker information. All virtual levels are designed to be very similar to off-line reconstruction, and are implemented in software. Full events are output from the HLT at a rate on the order of 100 Hz and are written to on-site data storage units for off-line analysis [16].

Figure 3-6 shows the algorithm utilized by all HLT virtual levels as well as off-line reconstruction. The algorithm begins when a τ jet candidate is passed to the HLT from the Level 1 trigger. An initial signal cone of opening angle ΔR_M is drawn around the axis of the trigger tower of the τ candidate. The cones used in this algorithm are defined in $\eta - \phi$ space and characterized by their half opening angle ΔR which is defined in Equation 3.5.

$$\Delta R \equiv \sqrt{\phi^2 + \eta^2} \tag{3.5}$$

The algorithm then examines any quality tracks that fall within the matching cone, and sorts these tracks by transverse momentum, p_T. The highest p_T track becomes the seed for the τ jet candidate. Next a signal cone is drawn around the four momentum vector of the τ candidate with an opening angle ΔR_S. The tracks within
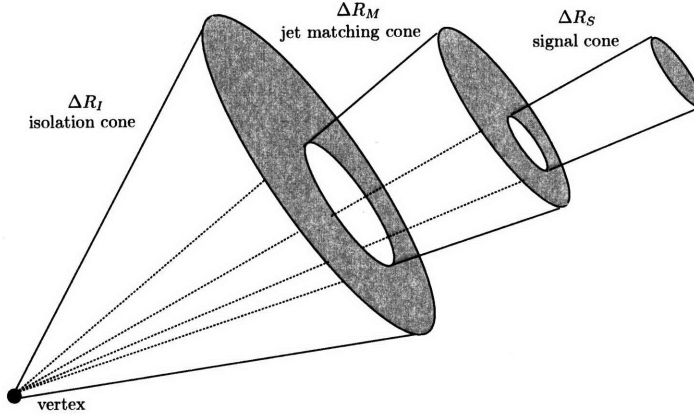
30

Figure 3-6: Schematic of the cones used by the HLT for identifying τ leptons.

the signal cone are again sorted by p_T, and the four momentum vector of the highest p_T track is added to the four momentum vector of the τ candidate. The signal cone is redrawn and the process repeats until all tracks within the signal cone have had their four momentum vector added to that of the τ candidate. This process ensures that the τ candidate is a highly collimated jet.

After the τ jet candidate has been created, an isolation cone with an opening angle ΔR_I is drawn around the vector of the τ candidate. The algorithm then searches for any quality tracks which fall within the isolation cone. If any tracks are found, the τ jet candidate is rejected. If no tracks are found, the τ candidate is tagged as a τ jet. The isolation cone ensures that the event is well isolated, which is a characteristic of τ jet topology and helps differentiate actual τ jets from faking jets [19].

Chapter 4

τ Identification

In order to develop a τ lepton identification algorithm, metrics must be defined which calculate the quality of the algorithm. Common metrics used to describe the quality of an identification algorithm are efficiency and fake rate. Here, the efficiency is the number of reconstructed τ jets from a Z, over the total number of real τ jets from a Z in the signal event. The fake rate is the number of reconstructed τ jets over the total number of reconstructed events in a background.

To obtain an efficiency and fake rate, both a signal sample and background sample are necessary. The Drell-Yan process provides the signal sample, requiring that the Z boson be on-shell within a mass window of $84 < M_Z < 98$ GeV which corresponds to 99% of all Z bosons in the signal sample [3]. The two most common backgrounds for the Drell-Yan process are simple two jet events (QCD events) and jets with a photon [20].

The particles of an event are generated using Pythia [21]. Pythia simulates particle decays through a pseudo-random process based on known branching ratios, but does not simulate the interaction of the particles with matter. Version 8.1 of Pythia is used. The particles generated by Pythia are then passed onto GEANT4, which simulates the interaction of the particles with the CMS detector [22]. Raw hits are output from GEANT4, simulated as hits within the CMS detector electronics, and reconstructed by the CMS reconstruction software (CMSSW) [23]. Version 1_3_1 of CMSSW is used for the reconstruction of samples. Within the CMS community these samples

Variable	Cut
$|\eta|$	< 2.3
leading track p_T	> 6 GeV
signal tracks	< 4
isolation tracks	= 0
τ charge	± 1
τ mass	< 1.8 GeV

Table 4.1: Table of cuts used in official τ selection.

are designated as "Spring 2007 MC".

4.1 Default Algorithm

The offline reconstruction of τ leptons is the same as in Section 3.3.2. A signal cone is drawn in $\eta - \phi$ space with $\Delta R_S = 0.10$ along with an isolation cone of $\Delta R_I = 0.45$, and the τ jet candidate must fulfill the requirements of Table 4.1.

The first cut on η from Table 4.1 requires that tracks fall within the fiducial region of the tracker, where full coverage is maintained. The second cut ensures that the leading track of the jet has sufficient transverse momentum for a well reconstructed track and a high energy deposition in the calorimeters. The third cut requires that the τ jet candidate must be either a one or three prong decay. By setting the number of tracks in the isolation cone to zero in the fourth cut, the algorithm ensures that the τ jet is isolated. The last two cuts ensure that the total charge and mass, calculated from the four momentum vector of the jet, fall within a range that is consistent with a τ jet.

4.1.1 Efficiency

Using the cuts of Table 4.1, and the definitions for signal and isolation cones given above, plots of the efficiency are shown in Figure 4-1. The two plots show the efficiency of the algorithm with respect to transverse energy and η. The efficiency with respect to the transverse energy has a clear turn on around 30 GeV and plateaus to approximately 50% for high energies. This behavior is understandable; as the τ jet
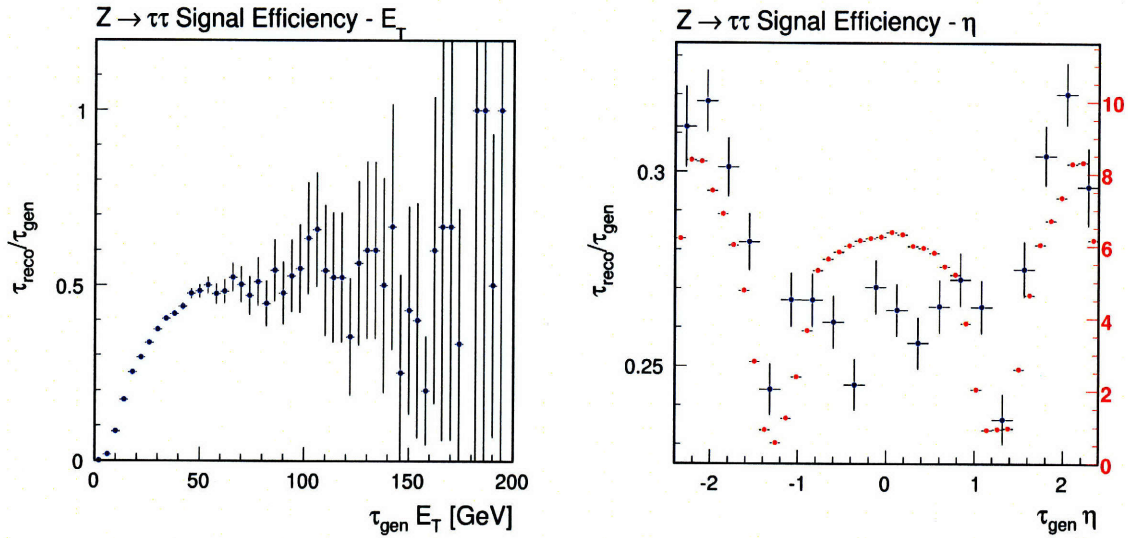
34

Figure 4-1: Plots of efficiencies in E_T (left) and η (right) space using the default CMS τ identification cuts. The η plot shows the efficiency in blue, and the average number of tracker hits per track in red.

has more transverse energy the more collimated it will become and subsequently the jet is more likely to pass the isolation and signal cone cuts.

The efficiency versus η also exhibits a significant structure which is not as well understood. A possible cause is the geometry of the silicon tracker with respect to η. The right plot of Figure 4-1 shows the relationship between the average number of silicon hits per track (red) and efficiency in η space (blue). While the average number of hits and efficiency are correlated, this is only one of many possible reasons behind the shape of the efficiency in η.

4.1.2 Fake Rate

The plots of Figure 4-2 show the fake rates for both the QCD and photons plus jets background. In general the QCD fake rate is nearly half that of the photons plus jets fake rate. Faking jets from the photons sample are matched to generator level data to find the composition of the faking jets. Only the final stable particles of the faking jets are considered and all intermediary particles are ignored. Table 4.2 shows the

Particle	≈ Percent
$\rho(770)^+$	30%
$\omega(782)$	25%
π^0	20%
$\rho(770)^0$	10%
π^+	8%
$K^*(892)^+$	7%

Table 4.2: Particles that fake a τ jet in the photons plus jets background along with their relative occurrence.
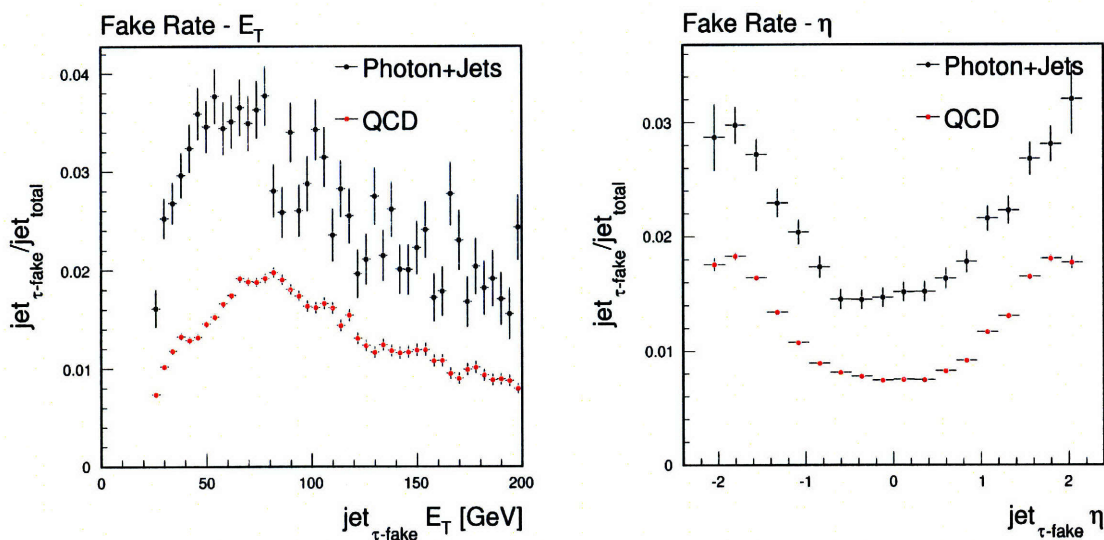

Figure 4-2: Plots of fake rates in E_T (left) and η (right) space using the default CMS τ identification cuts.

results.

As expected, the primary source of fake τ jets is from light hadrons, considering the composition of actual τ jets is also hadronic. A similar analysis of the QCD background sample was not performed due to lack of generator level information.

Another interesting feature that both the QCD and photon fake rate plots demonstrate is the convex parabolic shape in η space. One of the main reasons behind this shape is the definition of the cone size in $\eta - \phi$ space and the subsequent shrinking of the isolation cone in high η regions. This behavior is explored more in Section 4.2.
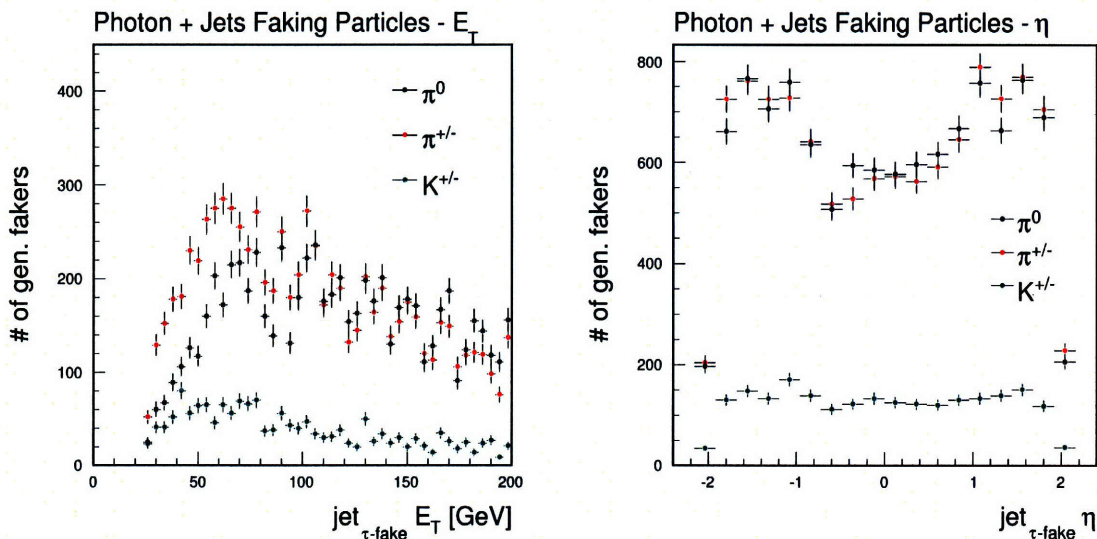
Figure 4-3: Plots of faking particles in E_T (left) and η (right) space using the default CMS τ identification cuts.

4.2 Proposed New Algorithm

The default algorithm suffers a series of drawbacks if it is to be used to identify τ leptons from a SM Higgs boson decay. Note first that the efficiency of the algorithm suffers severely with a slow turn on in the low E_T range, excluding a significant number of τ candidates. The low efficiency in η space of the central region of the detector also eliminates many τ candidates. Finally, the ratio between fake rate and efficiency is less then optimal. Either the fake rate needs to be decreased significantly or the efficiency raised.

4.2.1 Signal Cone

A first step in increasing the effectiveness of the algorithm is to examine how well the signal cone performs. The question arises as to whether the cone should be defined in $\eta - \phi$ space or in $\theta - \phi$ space. The angle in $\theta - \phi$ space is defined in Equation 4.1 and is also called the 3-D opening angle.

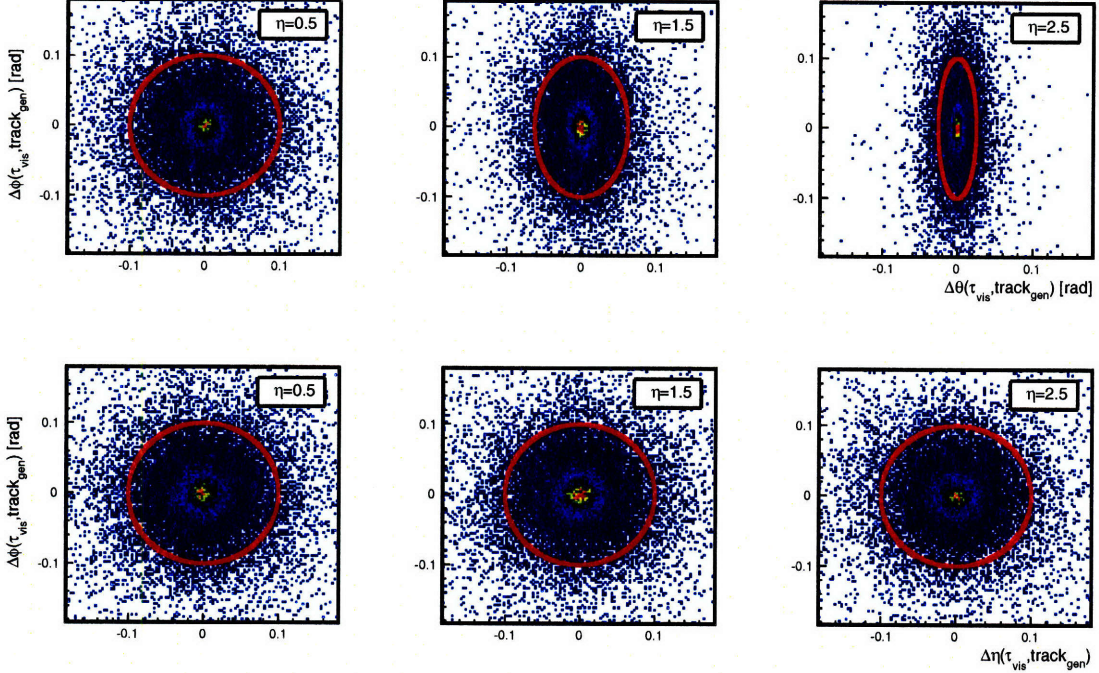$$\alpha \equiv \cos^{-1}(\cos\phi\cos\theta) \qquad (4.1)$$

37

Figure 4-4: Plot of generated τ jet topology in $\theta - \phi$ space (top) and $\eta - \phi$ space (bottom). The red line corresponds to $\Delta R_S = 0.10$.

Whether the signal cone should be defined by ΔR or $\Delta\alpha$ is dependent upon the underlying topology of the charged portion of the τ jet. Notice that for the 40% of τ decays that are one prong hadronic, this shape does not matter, because only one track is present in the tracker. However, for the 15% of the time that a τ decays with a three prong hadronic channel, the shape of the signal cone is important.

Using generator level information, the charged constituents of three prong hadronic τ decays are plotted with respect to the center of momentum of the τ jet. Figure 4-4 shows these plots, both in $\eta - \phi$ and $\theta - \phi$ space. The plots for each space are divided into three bins, $-0.5 < \eta < 0.5$, $0.5 < \eta < 1.5$, and $1.5 < \eta < 2.5$ which correspond to the range of η of the generated τ jet. The shape of the τ jet in $\theta - \phi$ space is dependent upon the η of the jet, opposed to $\eta - \phi$ space, where the shape is not dependent on η. A line defined by $\Delta R_S = 0.10$ is drawn on each plot to show the default CMS cut.

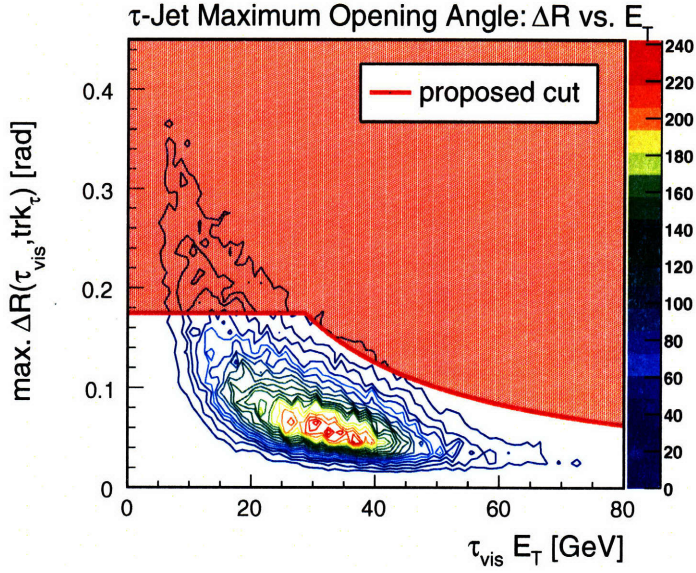To fully optimize the definition of the signal cone it is important to explore any

Figure 4-5: Maximum angle in ΔR between constituents of the τ jet and the center of the jet with respect to E_T of the visible τ. The colored contours indicate number of events.

possible parametrization of the topology of the τ jet, primarily, parametrization with respect to the transverse energy. Figure 4-5 gives the maximum angle between the center of the generated τ jet, and any charged constituent of the jet. The angle is defined by ΔR as this coordinate space is more natural for defining τ jets. As expected from the relativistic boost, τ jets at high E_T become more collimated. Equation 4.2 is a proposed cut to utilize the high E_T behavior, and is shown in red in Figure 4-5. A maximum ΔR cutoff at 0.17 is made to suppress fake rates with a minimal efficiency loss.

$$\Delta R_S = \min(0.17, 5/E_T) \tag{4.2}$$

4.2.2 Isolation Cone

While the signal cone is important, it only affects three prong decays which make up only 15% of all τ jets. The isolation cone however, affects both one and three prong
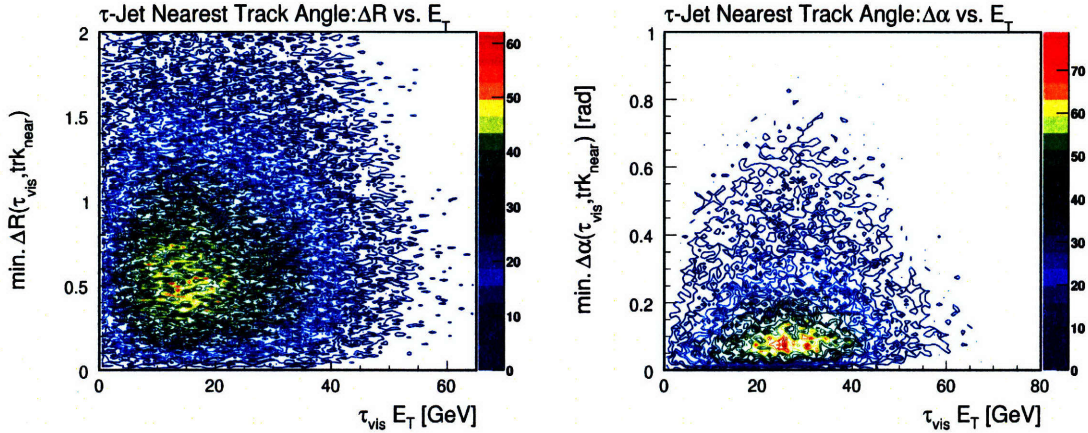
Figure 4-6: Minimum angle between the center of a τ jet and the nearest potential track with respect to the visible E_T of the τ jet. Angle is defined using ΔR (left) and $\Delta \alpha$ (right).

hadronic decays which correspond to 65% of all τ jets and plays a larger role in the selection efficiency. Like the signal cone, it is necessary to determine if the isolation cone should be defined in $\theta - \phi$ space or $\eta - \phi$ space. A clear structure like that in Figure 4-5 does not appear. The distribution of tracks in the signal sample that enter the isolation cone is uniform in both $\eta - \phi$ and $\theta - \phi$ space and does not give an advantage to either definition.

Examining the isolation cone size with respect to transverse momentum also does not give any insight. Figure 4-6 shows the angle between the closest non-τ jet track and the visible center of the τ jet using both ΔR and $\Delta \alpha$ for one prong hadronic decays. In both plots the contour colors correspond to number of events. Structure in both plots is present, but a strict cut in high E_T for both cases would eliminate τ jets important to new physics discoveries.

In Section 4.1 both the efficiency and fake rate display higher rates at large η, which indicates the τ jets in the central region are lost. The cause of this behavior stems from the definition of the shape of the isolation cone. Consider Figure 4-7. The left plot demonstrates the shape the cross section of the isolation cone takes at higher η. The blue circle traces out $\Delta R_I = 0.45$, the default CMS definition of the isolation cone with a center of $\eta = 0$. The green, gold, and red trace out the same $\Delta R_I = 0.45$
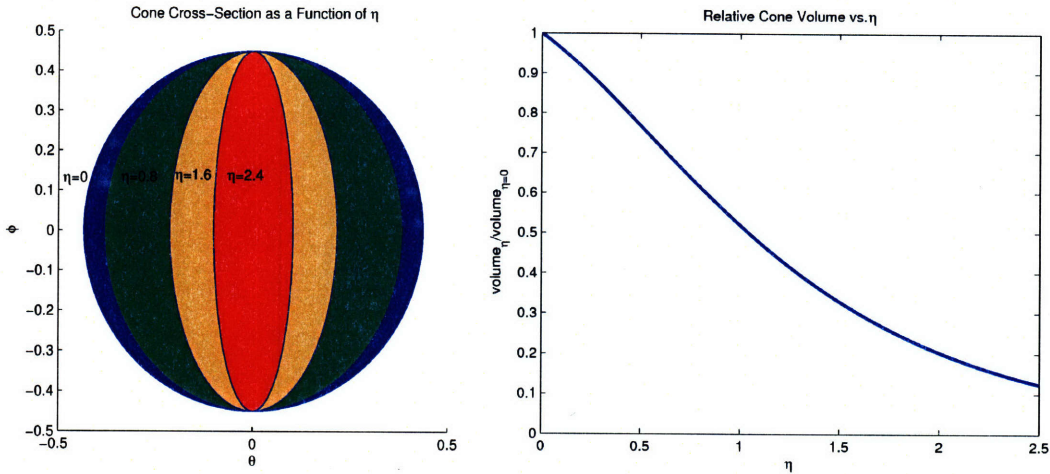
Figure 4-7: The plot on the left shows the shape of a cone with size $\Delta R = 0.45$ traced in $\theta - \phi$ space for varying η. The plot on the left gives the ratio of the volume of a cone at a given η with respect to the volume of a cone with $\eta = 0$.

for cones centered at η of 0.8, 1.6, and 2.4 respectively. At high η the cross section of the cone shrinks drastically. The right plot gives the fraction between the volume of a cone defined at a variable η with respect to the volume of the same cone defined at $\eta = 0$. Cones defined in $\eta - \phi$ space at $\eta > 2$ contain less then 20% of their volume at $\eta = 0$.

To avoid the problem of decreased efficiency in central regions an isolation cone can be drawn that is parametrized with respect to η such that it maintains a constant rejection of events with respect to the isolation cone cut.

Isolation cone rejection is dependent upon the density of non-signal tracks that enter the isolation cone. This density is shown in Figure 4-8. An isolation cone of size $\Delta R_I = 0.45$ and $\Delta \alpha_I = 0.45$ is drawn around generated τ lepton signals. All charged particles not belonging to the τ jet but within the isolation cone are then counted. The number of non τ jet tracks within the cone is divided by the volume of the cone, as defined in 3-D space. An arbitrary height is given to the cone and the results are normalized so that maximum density, ρ, is 1.

The density data points in both ΔR and $\Delta \alpha$ are fitted using Equation 4.3 with the parameters for the $\Delta \alpha$ fit given in Table 4.3. Except for very small η the $\theta - \phi$
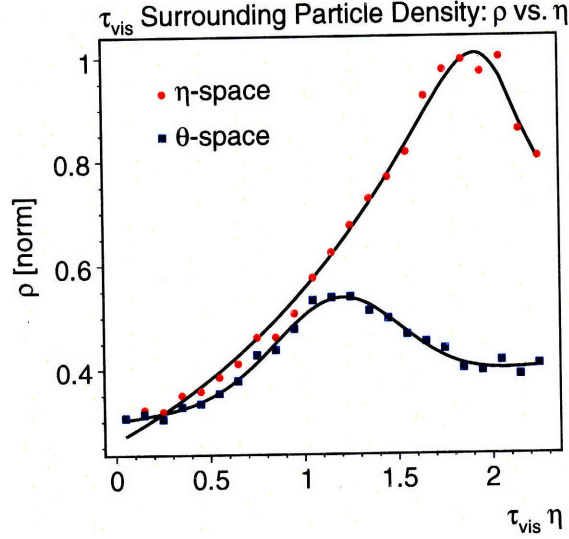
Figure 4-8: Density of potential tracks surrounding τ jets for varying η in both $\eta - \phi$ and $\theta - \phi$ space.

space always maintains a lower density, and rejects fewer τ candidates.

$$\rho(\eta) = a_1 e^{-\left(\frac{\eta - b_1}{c_1}\right)^2} + a_2 e^{-\left(\frac{\eta - b_2}{c_2}\right)^2} \tag{4.3}$$

For this reason the isolation cone is chosen to be represented in $\theta - \phi$ space with an opening angle defined by Equation 4.4 such that there is a flat efficiency with respect to η.

$$\alpha(\eta) = \sqrt{\frac{\rho_0}{\rho(\eta)}} \alpha_0 \tag{4.4}$$

Here, ρ_0 is the track density at $\eta = 0$ for θ space, shown in Figure 4-8. The constant α_0 is a free parameter that can be optimized. Finally $\rho(\eta)$ is given by Equation 4.3, the double Gaussian fit of the θ space density.

4.2.3   Optimization

Using Equation 4.2 to define the signal cone in $\eta - \phi$ space, and Equation 4.4 to define the isolation cone in $\theta - \phi$ space leaves the free parameter α_0 with the condition

42

Parameter	Value
a_1	0.18
b_1	1.18
c_1	0.47
a_2	0.53
b_2	7.37
c_2	9.80

Table 4.3: Parameter values obtained for the fit of the θ values of Figure 4-8 using Equation 4.3.
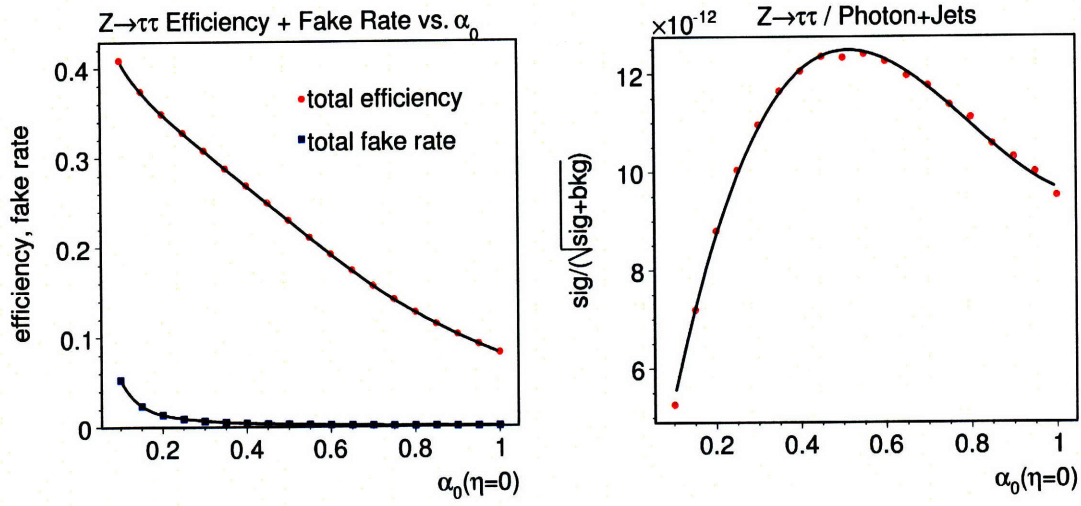

Figure 4-9: Total efficiency and fake rate with respect to the initial opening angle of the proposed algorithm α_0 (left) and the subsequent optimization of α_0 (right).

$\Delta\alpha_I > \Delta R_S$. The value for α_0 is found by optimizing the signal to background ratio, f, as given by Equation 4.5, where n_s is number of events in the signal, and n_{bg} is number of events in the background.

$$f = \frac{n_s}{\sqrt{n_s + n_{bg}}} \tag{4.5}$$

Figure 4-9 shows a plot of the efficiency of the signal ($Z \to \tau^+\tau^-$) along with the fake rate (photons plus jets) for varying α_0. For this optimization the QCD background was omitted. Fitting the data of Figure 4-9 and finding the maximum yields an optimal value of $\alpha_0 = 0.51$.

4.3 Comparison

While the proposed algorithm of Section 4.2 should maintain a constant efficiency with respect to η, it clearly does not. One possible reason is the density of charged tracks within the isolation cone from generator level information does not match the density from reconstructed tracks. The two plots of Figure 4-10 show the efficiencies of the default CMS algorithm in red ($\Delta R_I = 0.45, \Delta R_S = 0.10$) along with the proposed algorithm of Section 4.2 with $\alpha_0 = 0.51$ in green ($\Delta \alpha_I = \alpha(\eta), \Delta R_S = 5/E_T$). In the left plot with efficiency versus E_T, the efficiency of the proposed algorithm has a much earlier turn on, along with a more constant rate. However, the efficiency of the proposed algorithm does not match the default algorithm at high E_T. The right plot shows a behavior of the proposed algorithm that is nearly opposite of the default algorithm for efficiency versus η. The efficiency is not flat in η as expected, but it does give a high rate for the central regions of the detector.

To understand how well the proposed algorithm compares to the default algorithm, fake rates are given in Figure 4-11. Here there is a drastic improvement, with the fake rate being cut by a factor of nearly four. In the left plot, the parabolic shaped behavior of the default algorithm is not present in the proposed algorithm, which provides a flat fake rate with respect to η. Table 4.4 gives a brief overview of the total efficiencies and fake rates for the default algorithm. By varying the parameter α_0 the total efficiency of the proposed algorithm was matched with total efficiency of the default algorithm. The high E_T tail of the proposed algorithm was also matched to the default algorithm, again by varying the parameter α_0. The plots of Figure 4-12 show the efficiency and fake rate for the case of $\alpha_0 = 0.15$, with the high E_T regions of the efficiencies matched. While varying α_0 from the optimal value found in Section 4.2 does lead to a less efficient algorithm, this still allows the power of the proposed method to be seen.

Algorithm	Efficiency	Fake Rate
Default	27.7%	1.96%
Proposed $\alpha_0 = 0.40$	26.9%	0.44%
Proposed $\alpha_0 = 0.15$	37.4%	2.36%

Table 4.4: Total efficiencies and fake rates for the default algorithm, the proposed algorithm with a matched total efficiency, and the proposed algorithm with a matched high E_T efficiency.
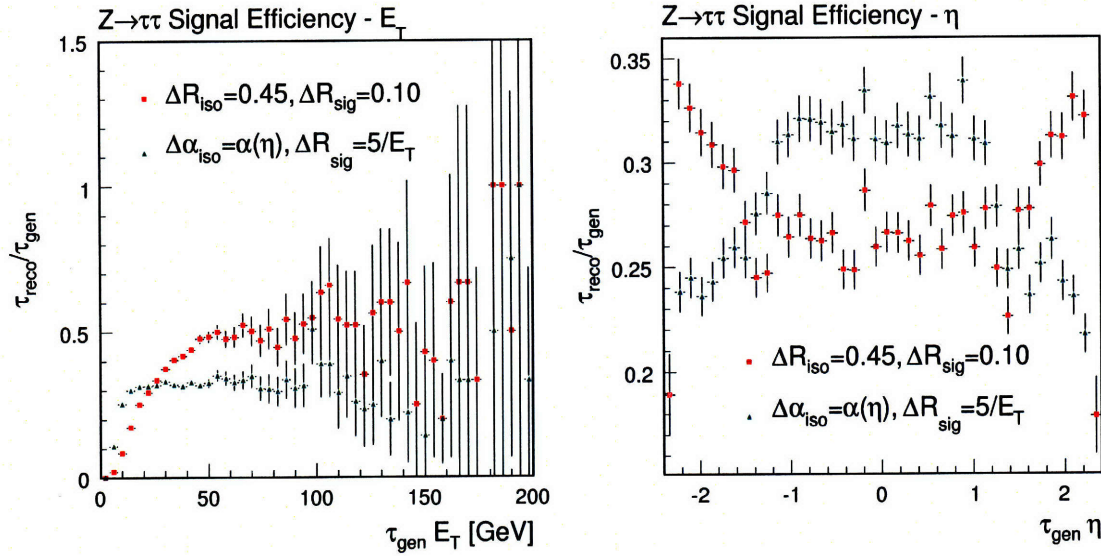

Figure 4-10: Plots of efficiencies in E_T (left) and η (right) space using default CMS cuts and new cuts.
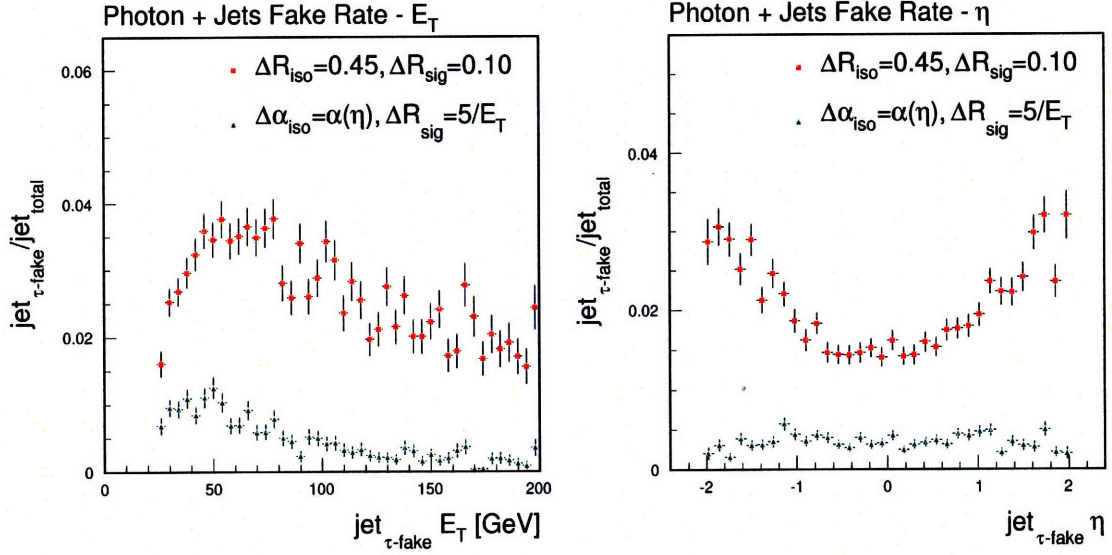
Figure 4-11: Plots of photon plus jets fake rates in E_T (left) and η (right) space using default CMS cuts and new cuts.
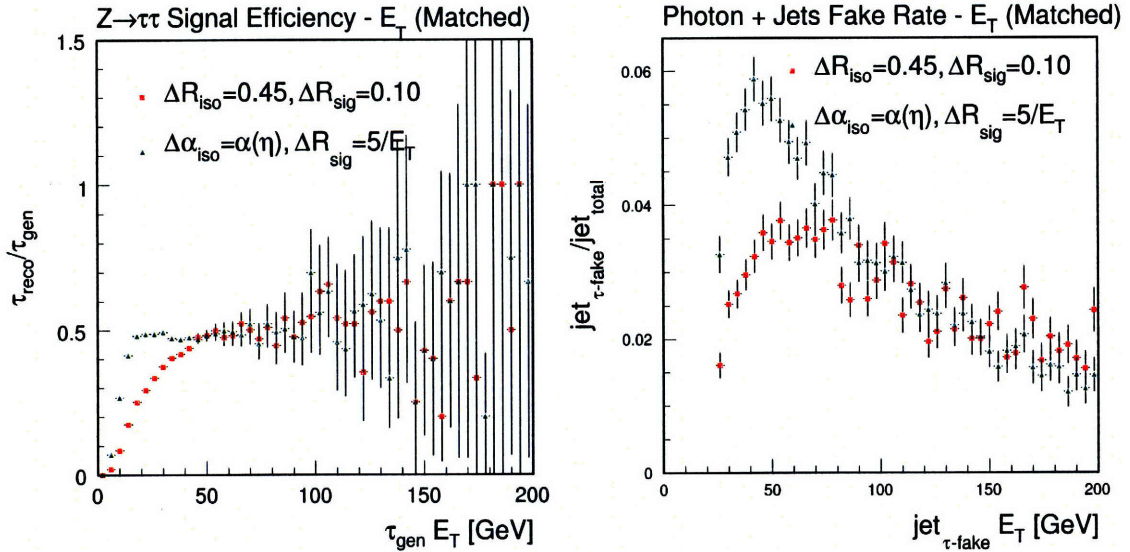

Figure 4-12: Plots of efficiencies in E_T (left) and η (right) space using default CMS cuts and proposed cuts matched to default cuts in high E_T.

Chapter 5

Conclusion

A variety of approaches is taken in an attempt to improve the efficiency and decrease the fake rates of τ lepton identification. The proposed algorithm gives a strong argument for a definition of the signal cone in $\eta-\phi$ space based on topological evidence of generator level information from τ jets. A strong argument for parametrization of the signal cone with respect to transverse energy of the visible τ jet is also given based on generator level information. Finally, the advantages for some physics searches with an isolation cone parametrization based on charged particle density is given.

While these changes in both signal cone and isolation cone definition do increase efficiencies and decrease fake rates, it is important to note the energy ranges in which these changes occur, primarily in the lower energy range of τ jets. This demonstrates that the methods used for τ lepton identification have to be adjusted to the signal sample being used. A wide range of analysis with τ leptons exist which require different τ characteristics, and so a range of identification techniques should be made available.

Bibliography

[1] W. Cottingham and D. Greenwood, *An Introduction to the Standard Model of Particle Physics*, ch. 1 - The particle physicist's view of nature. Cambridge University Press, second ed., 2007.

[2] R. Mohapatra and et al, "Theory of neutrinos: A white paper," *arXiv*, pp. 1–143, Dec 2005.

[3] W.-M. Yao and et al, "Review of Particle Physics," *Journal of Physics G*, vol. 33, pp. 1+, 2006.

[4] R. Eisberg and R. Resnick, *Quantum Physics of Atoms, Molecules, Solids, Nuclei, and Particles*, ch. 18 - More Elementary Particles. John Wiley and Sons, Inc, second ed., 1985.

[5] R. Feynam and M. Grill-Mann, "Theory of fermi interaction," *Physical Review*, vol. 109, pp. 193–199, Jan 1958.

[6] D. Abbaneo and et al, "The LEP electroweak working group," 2003.

[7] E. Accomando and et al, "Physics with e^+e^- linear colliders," *Physics Reports*, vol. 299, pp. 1–78, Jun 1998.

[8] M. Spira and et al, "QCD effects in Higgs physics," *Fortschritte der Physik*, vol. 46, pp. 203–284, Apr 1999.

[9] J. Poole, *LHC Design Report*, vol. 1 - Machine, ch. 1 - Introduction. CERN EDMS, 445829 v.4 ed., 2008. Internal CMS Document.

[10] J. Poole, *LHC Design Report*, vol. 1 - Machine, ch. 3 - Layout and Performance. CERN EDMS, 445831 v.5 ed., 2008. Internal CMS Document.

[11] J. Poole, *LHC Design Report*, vol. 1 - Machine, ch. 2 - Beam Parameters and Definitions. CERN EDMS, 445830 v.5 ed., 2008. Internal CMS Document.

[12] CMS Collaboration, "The CMS experiment at the CERN LHC," *Journal of Instrumentation (Draft)*, p. 261, 2008. Detector report draft.

[13] United States CMS Collaboration, "United States Compact Muon Solenoid picture archive," 2008.

[14] CMS Collaboration, "The electromagnetic calorimeter project technical design report," CMS TDR 4, CERN European Laboratory for Particle Physics, Geneva, Switzerland, Dec 1997.

[15] CMS Collaboration, "The muon project technical design report," CMS TDR 3, CERN European Laboratory for Particle Physics, Geneva, Switzerland, Dec 1997.

[16] C. Seez and CMS Collaboration, "The CMS trigger system," *European Physical Journal*, vol. 34, pp. 151–159, Aug 2003.

[17] C. Paus, "Private communication," 2008.

[18] C. Foudas, "Level 1 triggers at CMS," 2007. Tau Workshop, Pisa, 8.6.07.

[19] S. Gennai and et al, "Tau jet reconstruction and tagging at high level trigger and off-line," *CMS Internal Note*, Jan 2006.

[20] S. Abdullin and et al, "Summary of the CMS potential for the Higgs boson discovery," *European Physics Journal C*, vol. 39, pp. 41–61, Feb 2005.

[21] T. Sjöstrand and et al, "Pythia," 2008.

[22] A. Kimura and et al, "Geometry and tracking software - version 4," 2008.

[23] D. Lange and et al, "Compact Muon Solenoid software," 2008.